

The Mean and the Time Variability of the Shallow Meridional Overturning Circulation in the Tropical South Pacific Ocean

N. V. ZILBERMAN, D. H. ROEMMICH, AND S. T. GILLE

Scripps Institution of Oceanography, University of California, San Diego, La Jolla, California

(Manuscript received 27 February 2012, in final form 13 September 2012)

ABSTRACT

The meridional transport in the Pacific Ocean subtropical cell is studied for the period from 2004 to 2011 using gridded Argo temperature and salinity profiles and atmospheric reanalysis surface winds. The poleward Ekman and equatorward geostrophic branches of the subtropical cell exhibit an El Niño–Southern Oscillation signature with strong meridional transport occurring during La Niña and weak meridional transport during El Niño. At 7.5°S, mean basinwide geostrophic transport above 1000 dbar is 48.5 ± 2.5 Sv ($\text{Sv} \equiv 10^6 \text{ m}^3 \text{ s}^{-1}$) of which 30.3–38.4 Sv return to the subtropics in the surface Ekman layer, whereas 10.2–18.3 Sv flow northward, feeding the Indonesian Throughflow. Geostrophic transport within the subtropical cell is stronger in the ocean interior and weaker in the western boundary during La Niña, with changes in the interior dominating basinwide transport. Using atmospheric reanalyses, only half of the mean heat gain by the Pacific north of 7.5°S is compensated by oceanic heat transport out of the region. The National Oceanography Centre at Southampton air–sea flux climatology is more consistent for closing the oceanic heat budget. In summary, the use of Argo data for studying the Pacific subtropical cell provides an improved estimate of basinwide mean geostrophic transport, includes both interior and western boundary contributions, quantifies El Niño/La Niña transport variability, and illustrates how the meridional overturning cell dominates ocean heat transport at 7.5°S.

1. Introduction

The shallow meridional overturning circulation, also known as the subtropical cell (STC), controls the transfer of mass, heat, and salt between the subtropics and the equator and, as such, plays a key role both in the redistribution of water properties in the ocean and in oceanic climate variability. In the Pacific Ocean, the STC consists of subtropical water subducted in eastern areas of the ocean, flowing westward and equatorward in the upper pycnocline layers through both western boundary and interior pathways. The STC is closed by upwelling at the equator, with return flow to the subtropics in the surface Ekman layer. The time variability of the STC is mainly driven by wind forcing (McCreary and Lu 1994; Lu et al. 1998). Spinup and spindown of the subtropical gyres due to modifications of the wind stress curl lead to changes in the strength of the equatorward geostrophic flow (Kleeman et al. 1999). Geostrophic transport anomalies

affect the sea surface temperature (SST) at the equator by way of cold water upwelling (Klinger et al. 2002) and temperature advection from the extratropics (Gu and Philander 1997). Anomalies in the SST in turn lead to changes in the wind stress curl and poleward Ekman transport (Alexander et al. 2002).

The interior pathway of subtropical waters to the equator in the Pacific Ocean carries three times as much volume transport in the Southern Hemisphere as in the Northern Hemisphere (Johnson and McPhaden, 1999). According to Johnson and McPhaden (1999), two factors contribute to larger equatorward transport in the Southern Hemisphere. First, the high potential vorticity region located under the intertropical convergence zone (ITCZ) reroutes Northern Hemisphere water to the western boundary. Second, the region of large subduction rate in the Southern Hemisphere has about twice the area of the equivalent region in the Northern Hemisphere and correspondingly twice the magnitude of subduction. The intent of this study is to provide an improved estimate of the geostrophic and Ekman transports across the tropical South Pacific Ocean and to study the time variability of the volume transport at the western boundary and in the interior.

Corresponding author address: Nathalie Zilberman, Scripps Institution of Oceanography, University of California San Diego, 9500 Gilman Drive, La Jolla, CA 92093-0230.
E-mail: nzilberman@ucsd.edu

This study is driven by three scientific questions. The first is focused on evaluating interannual variability of the volume transport toward the equator. Observations (McPhaden and Zhang 2002) and numerical simulations (Capotondi et al. 2005) have documented a decrease in the equatorward pycnocline transport in the interior from the mid-1970s to the mid-1990s. McPhaden and Zhang suggest that this trend is related to the decreased frequency of La Niña events and the increased frequency, duration, and magnitude of El Niño events since 1976–77. Since the mid-1990s, the Pacific Ocean appears to be experiencing a new shift characterized by a re-intensification of the STC (McPhaden and Zhang 2004; Cheng et al. 2007). The factors initiating the atmospheric circulation changes are unknown. Whether the El Niño–Southern Oscillation (ENSO) cycle is altered by or affects the Pacific decadal oscillation is an open question. At interannual time scales, numerical simulations indicate that the geostrophic transport in the interior is anticorrelated with the El Niño-4 index (Lohmann and Latif 2005). Interannual variations of the sea level anomalies in the western Pacific were investigated by Melet et al. (2010), who used altimeter data to estimate the magnitude of the western boundary current. The authors found that, at the western boundary, the geostrophic transport within the surface layer is anticorrelated with the Southern Oscillation index. Numerical simulations suggest that the depth-integrated western boundary transport is anticorrelated with the interior (Lübbecke et al. 2007; Lee and Fukumori 2003). A goal for the present work is to quantify the interannual variability of volume transports in the interior and at the western boundary with direct observations.

A second motivation for this work is to achieve a better understanding of southern sources of the Indonesian Throughflow (ITF). Numerical simulations of the ITF time variability have shown interannual changes in ITF volume transport to be induced by the Pacific trade winds during ENSO events (Tillinger and Gordon 2009; Potemra and Schneider 2007). Conversely, numerical simulations of the coupled ocean–atmosphere system have shown that interannual variations of the ITF volume transport induce changes in the mean oceanic and atmospheric conditions in the tropical Pacific Ocean (Song et al. 2007; Santoso et al. 2011). Johnson and McPhaden (2001) examined conductivity–temperature–depth (CTD) recorder/Acoustic Doppler Current Profiler (ADCP) sections across the equator in the interior Pacific Ocean. Velocities showed stronger subsurface poleward flow and weaker equatorward thermocline flow in the Northern Hemisphere compared with the Southern Hemisphere. They found that 10 Sv ($\text{Sv} \equiv 10^6 \text{ m}^3 \text{ s}^{-1}$) of Southern Hemisphere thermocline water upwell at the equator and travel northward

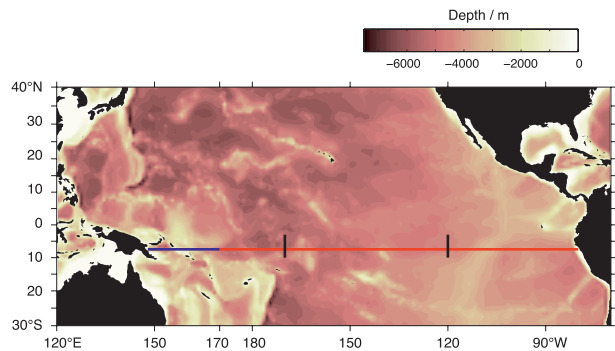


FIG. 1. Zonal sections across the Solomon Sea region (blue line) and interior Pacific Ocean (red line) and meridional sections at 170° and 120°W (black lines). The underlying color gives the 2° gridded elevations/bathymetry for the world (ETOPO2).

as surface water. This interhemispheric volume transport from the southern to the northern Pacific Ocean has a magnitude comparable to local estimates of the ITF (Gordon 2005; Sprintall et al. 2009). The findings of Johnson and McPhaden (2001) suggest that the interior transport of the STC in the southern Pacific provides a measure of the volume transport from the Pacific to the Indian Ocean.

The third motivation for this work is to quantify the oceanic heat budget in the Pacific Ocean north of 7.5°S, both for the mean and ENSO variability. Roemmich and Gilson (2011) investigated the ENSO-related variability in oceanic heat content, finding that global heat content between 0 and 500 m increases during La Niña and decreases during El Niño, by $\sim 1 \text{ W m}^{-2}$. Consistent with this, the numerical study by Cheng et al. (2007) found that, as colder waters upwell in the equatorial Pacific when the STC strengthens, heat gain by the ocean via air–sea flux also increases. Our goal is to evaluate the poleward heat transport related to the STC in the tropical South Pacific Ocean and to consider whether variations of the ocean heat transport are balanced by air–sea heat exchange anomalies at interannual time scales.

In this work, the time variability of the shallow meridional overturning circulation in the tropical South Pacific Ocean is described over the 2004–11 period using Argo data and wind products from Quick Scatterometer (QuikSCAT), the National Centers for Environmental Prediction (NCEP), and the European Centre for Medium-Range Weather Forecasts (ECMWF) Re-Analysis (ERA). The principal focus is on geostrophic and Ekman transport computed at 7.5°S. This latitude was chosen to maximize the Argo float spatial coverage. Time series are presented for the volume transport in the Solomon Sea region and in the interior Pacific Ocean (Fig. 1). The role of the STC in the heat budget of the tropical Pacific is examined. In the following section, the datasets used in this study are described. The results are presented in two parts. First,

estimates of the geostrophic and Ekman transports at 7.5°S and the northward volume transport feeding the ITF are presented (section 3). Second, the contribution of the geostrophic flow and the wind to the heat budget in the tropical Pacific are described (section 4). A summary and conclusions follow (section 5).

2. Observations

a. Argo float profiles

Temperature and salinity profiles are provided by the Argo Global Data Assembly Center. For this study both real-time quality-controlled and delayed-mode quality-controlled data are used. For float measurements that have not yet undergone delayed-mode adjustment, an additional quality control test is carried out in order to eliminate profiles containing measurement anomalies and cases where instrument failures are detected. Roemmich and Gilson (2009) provide a description of this additional evaluation.

The Argo profiles are linearly interpolated onto 56 pressure levels between 0 and 2000 dbar with a vertical resolution of 10 dbar near the surface increasing to 100 dbar at depth. An 8-yr mean field mapped to a $\frac{1}{2}^\circ \times \frac{1}{2}^\circ$ grid is estimated for each month using a least squares fit of 300 neighboring points. Anomaly fields are calculated using objective analysis for each of the 96 months of the time series. The mean and the anomaly fields are then interpolated onto a $1^\circ \times 1^\circ$ grid. Roemmich and Gilson describe the Argo profile mapping in detail. In this work, we use gridded Argo data for the January 2004 to December 2011 period, and unless otherwise specified all of our analysis is for the full 8-yr period. The gridded temperature and salinity data are currently available on the Argo website (<http://www.argo.ucsd.edu>). The monthly mean and anomaly fields of temperature and salinity across the tropical Pacific Ocean are used to calculate geostrophic velocity. In a highly stratified region such as the tropical Pacific, some floats are unable to vary their buoyancy sufficiently to profile below 1000 m (Kobayashi and Minato 2005). Therefore, below 1000 m the gridded data products are derived using fewer profiles. In the following, we focus on the data recorded within the 0–1000-m depth range to provide maximal spatial and temporal coverage.

Argo floats drift passively, mostly at 1000-m depth, and tend to follow water mass pathways defined by ocean currents. Although the floats have provided broad spatial coverage of the Pacific Ocean since 2004, the float sampling density at the western boundary of the tropical South Pacific is heterogeneous. In regions such as the Solomon Sea, where the sampling is not dense enough to fully resolve the flow field, interpolation attenuates

the density gradients and therefore reduces the time-varying currents. To improve the mean and the anomaly fields in the Solomon Sea, we consider an additional grid constructed using 99 neighboring points instead of 300 in the least squares fit. The outermost radius of smoothing in the Solomon Sea is 6° – 8° using 300 points in the least squares fit and 2° lower using 99 points. While the finer grid allows us to observe some finer-scale variability, the resulting transport estimates in the Solomon Sea have larger uncertainties than the interior and should be interpreted with caution. The important western boundary current region is the subject of glider and hydrographic sampling, and our results based on Argo can be compared for consistency with those independent observations.

b. Climatological products

Reanalysis has proven to be a key tool for merging observations in a dynamically consistent way to obtain a best estimate of atmospheric conditions, even in regions where observations are sparse or discontinuous. For example, for this study the QuikSCAT provided a useful measurement of surface winds until it stopped working in November 2009. The NCEP and ECMWF reanalyses provide estimates of wind field and surface heat fluxes based on remaining data sources after the QuikSCAT mission ended. In the case of volume and heat transport calculations where uncertainties arising from the limitations of the observations and analysis systems are significant, the use of multiple products provides a range of estimates. In this study, both NCEP and ECMWF are used to calculate the Ekman transport and the heat flux. In an attempt to evaluate the reanalyses against observations, the wind field estimates computed using the NCEP and ECMWF datasets are compared with a QuikSCAT product over the 2004–09 period. In addition, the air–sea flux estimates using NCEP and ECMWF are compared with the inverse analysis of the National Oceanography Centre at Southampton (NOCS) air–sea flux climatology, version 1.1a (Grist and Josey 2003).

The NCEP fields are taken from the NCEP–National Center for Atmospheric Research (NCAR) archive. Data are available from the NCEP website (<http://www.esrl.noaa.gov>). The NCEP model version considered in this work uses a T62 Gaussian grid, which corresponds to a horizontal resolution of approximately 200 km. Kalnay et al. (1996) described the NCEP–NCAR 40-yr reanalysis project in detail. The momentum flux, surface sensible heat flux, surface latent heat flux, net longwave radiation, and net shortwave radiation are taken from the NCEP–NCAR monthly means of 6-hourly data.

The ECMWF fields are taken from the interim ECMWF Re-Analysis (ERA-Interim) archive available on the ECMWF website (<http://data-portal.ecmwf.int/>). The

ERA-Interim reanalysis uses a T255 grid, which corresponds to an effective grid resolution on the order of 100 km. Berrisford et al. (2009) described the ERA-Interim reanalysis. The instantaneous surface stress is taken from the ECMWF monthly means of daily mean fields. The surface sensible heat flux, surface latent heat flux, surface solar radiation (shortwave radiation), and surface thermal radiation (longwave radiation) are taken from the ECMWF synoptic monthly mean archives.

The QuikSCAT fields are taken from the Center for Ocean–Atmospheric Prediction Studies archive (<http://coaps.fsu.edu/>) at the Florida State University. The QuikSCAT datasets used in this study are monthly fields of pseudostress and wind speed at 10-m height projected onto a $0.5^\circ \times 0.5^\circ$ grid. The method used to generate the pseudostress fields is described by Pegion et al. (2000). The wind products are converted into wind stress using the Large et al. (1994) formulation for the neutral stability drag coefficient [see Eqs. (A1a)–(A1c) in their appendix].

The NOCS climatology provides air–sea heat fluxes generated using an inverse method constrained by hydrographic estimates of ocean heat transport for the 1980 to 1993 time period (Grist and Josey 2003). Data are available from the NOCS (http://www.noc.soton.ac.uk/noc_flux/). The sensible heat flux, latent heat flux, longwave flux, and shortwave flux are taken from the $1^\circ \times 1^\circ$ NOCS1.1a flux monthly means archive.

All of these products have limitations. Validation of NCEP and ECMWF against observations has been considered by Bentamy et al. (2003) and by Risien and Chelton (2008). Although atmospheric reanalyses are shown to give predictions in broad agreement with observations, the reliability of the NCEP and ECMWF estimates for the wind field and surface heat fluxes is reduced in specific regions. Comparisons between QuikSCAT observations and ECMWF analyses show that the 10-m wind estimates from both NCEP and ECMWF are biased compared to QuikSCAT observations in regions of strong ocean currents (Chelton and Freilich 2005). Also, compared to QuikSCAT measurements, the NCEP and ECMWF analyses underestimate the variability of the wind field in regions of strong jets and SST fronts (Chelton et al. 2006). Additional limitations of NCEP and ECMWF include their reduced skill at representing heat losses from western boundary currents (Moore and Renfrew 2002; Rouault et al. 2003). Uncertainties remain in the amplitude and interannual variability of precipitation and outgoing longwave radiation across the warm pool of the western Pacific in the NCEP and ECMWF analyses (Shinoda et al. 1999; Newman et al. 2000). Finally, the ability of the NCEP and ECMWF models to provide accurate estimates of surface heat fluxes in regions of strong winds is limited (Renfrew

et al. 2002). ERA-Interim, the latest ECMWF global atmospheric reanalysis, presents an improvement in the representation of the hydrological cycle over the 40-yr ECMWF Re-Analysis (ERA-40) (Dee et al. 2011). In the tropics, ERA-Interim generally captures better the magnitude and the variability of net surface heat fluxes than NCEP (Kumar et al. 2012). Comparisons between air–sea fluxes generated using the inverse analysis of the NOCS climatology and NCEP and ECMWF indicate an imbalance in the global heat flux budget higher than 5 W m^{-2} in the reanalysis products (Grist and Josey 2003). There are ongoing efforts to improve the NCEP and ECMWF analyses through changes to data input, bulk flux algorithms, data sampling, and analysis procedures (Brunke et al. 2011; Decker et al. 2011). In this work, we assess whether NCEP or ECMWF gives volume transport and surface heat fluxes most consistent with the Argo data.

Satellite altimetry products by Segment Sol multi-missions d'Altimétrie, d'Orbitographie et de localisation précise/Data Unification and Altimeter Combination System (Ssalto/Duacs) are used as a means to study the geostrophic transport in regions where the Argo float sampling is reduced. The Ssalto/Duacs fields used here are delayed time weekly fields of altimetric height anomaly projected onto a $1/3^\circ \times 1/3^\circ$ grid.

3. Velocity and transport across 7.5°S

Acceleration potential contours are streamlines of relative geostrophic velocity on specific volume anomaly surfaces (Montgomery 1937; McDougall 1989) and as such give a useful representation of the flow field. Figure 2a shows acceleration potential contours relative to 1000 dbar, as in McDougall [1989, Eq. (15)], averaged over the 2004 to 2011 time period on the specific volume anomaly surface $306 \times 10^{-8} \text{ m}^3 \text{ kg}^{-1}$. This specific volume anomaly surface is chosen because it corresponds to the middle of the equatorial pycnocline, close to the potential density surface 1025 kg m^{-3} (Fig. 3).

In the South Pacific, the South Equatorial Current (SEC) on this specific volume surface is seen in streamlines running from the outcropping region in the southeast toward the west and northwest. The northwestward flows are stronger in the eastern half of the basin, showing the direct pathway from the outcrop region to the equator. Farther south the SEC streamlines extending westward bifurcate at the Australian coast. Here the northward extension of the SEC is the North Queensland Current, which follows the coast, eventually becoming the New Guinea Coastal Undercurrent (NGCU) in the Solomon Sea. In this analysis, we consider two regions within the tropical South Pacific Ocean: the Solomon Sea

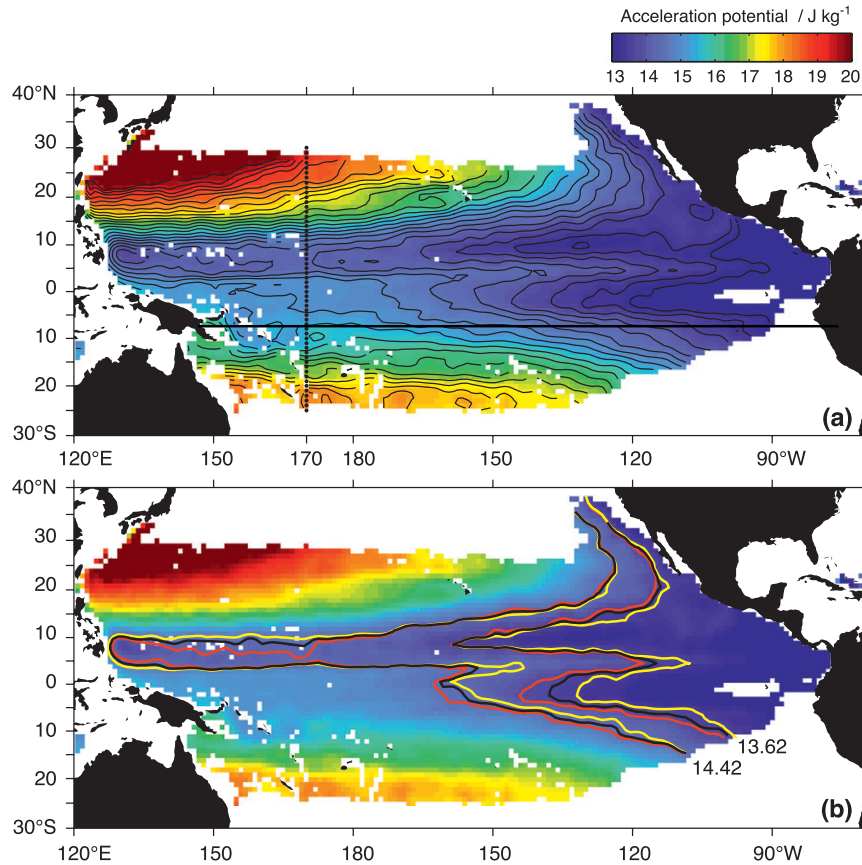


FIG. 2. (a) Acceleration potential contours relative to 1000 dbar averaged from 2004 to 2011 on the mean steric anomaly surface $306 \times 10^{-8} \text{ m}^3 \text{ kg}^{-1}$. Contour interval is 0.4 J kg^{-1} . (b) Acceleration potential contour 13.62 and 14.42 J kg^{-1} averaged from 2004 to 2011 (black), and for La Niña events (red) and El Niño events (yellow) on the mean steric anomaly surface $306 \times 10^{-8} \text{ m}^3 \text{ kg}^{-1}$. The dashed line at 170°E indicates the limit between the Solomon Sea region and the interior. The continuous line is at 7.5°S .

region, from the New Guinea coast to 170°E (blue line in Fig. 1), and the interior Pacific, from 170°E to the South American coast (red line in Fig. 1).

Figure 2b highlights two of the acceleration potential contours, 13.62 and 14.42 J kg^{-1} on the midpycnocline specific volume anomaly surface. In the Southern Hemisphere the 2004–10 mean transit time for water to reach the equator from the outcrop region is 2 yr along both 13.62 and 14.42 J kg^{-1} streamlines. This is one-fifth of the time needed in the Northern Hemisphere (Fig. 2b) on the same streamlines. The mean transit time is computed using the length of the acceleration potential contour and the geostrophic velocity averaged over the 8-yr time period. This large hemispheric asymmetry in transit times is due to two factors. First, these surfaces outcrop at lower latitude in the southeast Pacific (10° – 15°S) than in the northeast Pacific (35°N). Second, in the Northern Hemisphere the ventilated subtropical waters in the interior Pacific deviate to the west around the high vorticity region under the

intertropical convergence zone before reaching the equator. In contrast, the ventilated waters in the Southern Hemisphere travel from the outcrop region directly to the equator. The consequence of both of these factors—that equatorial waters originating in the south are much more recently ventilated than those from the north—is in agreement with Johnson and McPhaden (1999).

The midpycnocline streamlines in the Southern Hemisphere vary with the ENSO cycle. East of the date line, La Niña streamlines near the equator are offset toward the west from their mean position, with this westward offset increasing toward the east. This means that the acceleration potential contours are closer to one another during La Niña, indicating an increase in westward and northward flow within the SEC during La Niña compared to El Niño. The Niño-3.4 index used in this work is based on the NOAA Optimal Interpolation SST (OISST) for the 30-yr period 1981–2011 in the region 5°S – 5°N , 190° – 240°E (http://www.emc.ncep.noaa.gov/research/cmb/sst_analysis/).

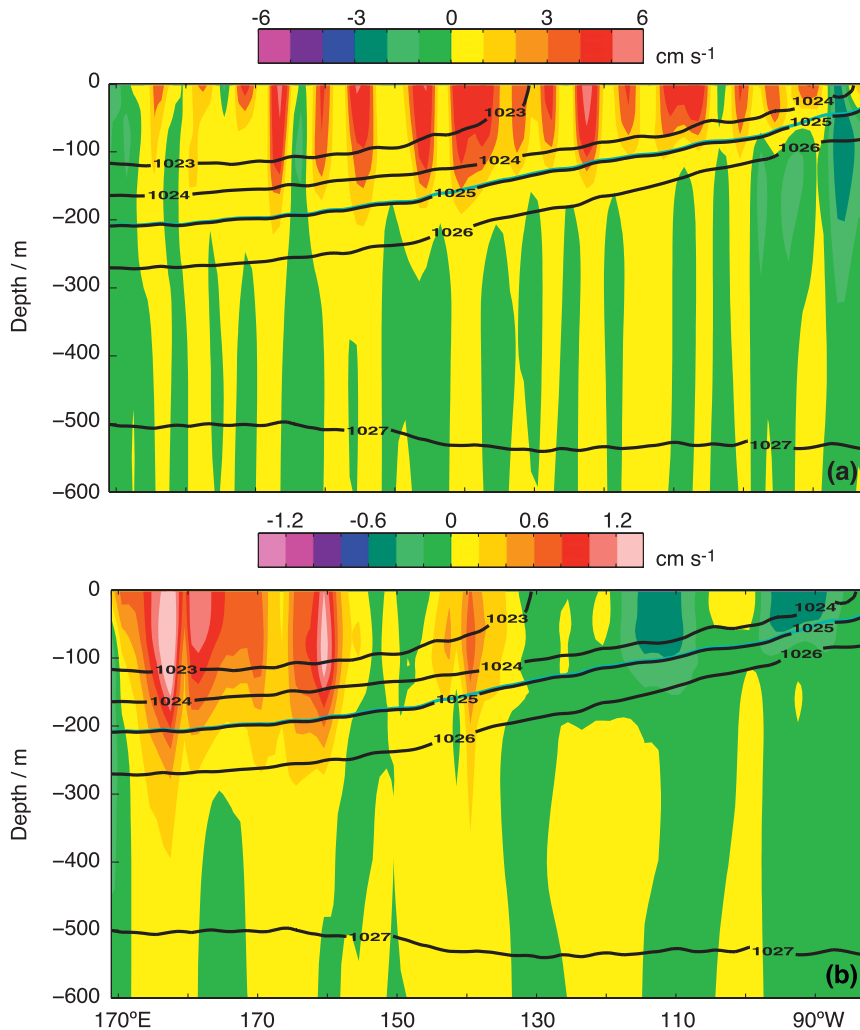


FIG. 3. Meridional geostrophic velocity v_g in the interior at 7.5°S (a) averaged from 2004 to 2011 and (b) the v_g anomaly for La Niña events. The black lines correspond to 2004–11 mean density contours (kg m^{-3}). The blue line corresponds to the 2004–11 mean steric anomaly surface $306 \times 10^{-8} \text{ m}^3 \text{ kg}^{-1}$.

By El Niño conditions, we refer to times when the 12-month running mean of the Niño-3.4 index exceeds 0.25. La Niña conditions correspond to a Niño 3.4 index lower than -0.25 . We recognize that the 2004 to 2011 time period is limited with only three El Niño and three La Niña episodes. However, the 8-yr Argo record effectively captures the patterns of ENSO variability seen in much longer time series of temperature, salinity, and steric height (Roemmich and Gilson 2011).

a. Geostrophic velocity and transport

1) THE OCEAN INTERIOR

The meridional geostrophic velocity relative to 1000 m at 7.5°S in the ocean interior, averaged from 2004 to

2011, is shown in Fig. 3a. Geostrophic transport estimates relative to 1500 m are similar (Fig. 5a), and the mean velocity at 1000 m from Argo trajectory data is not significantly different from zero. West of 100°W the geostrophic velocity is mostly equatorward ($v_g > 0$), consistent with the deepening of the pycnocline from east to west. The strongest velocities are seen east of 170°W in the surface layer. East of 100°W the geostrophic velocity is largely southward below the 1025 kg m^{-3} isopycnal. The elevated southward velocities ($v_g < -0.01 \text{ m s}^{-1}$) in the upper 200 m are the signature of the Peru–Chile Undercurrent (PCU) (Silva and Neshyba 1979; Montes et al. 2010). During La Niña events of the 2004–11 period, increased northward flow occurs west of 120°W and increased southward flow east of 120°W

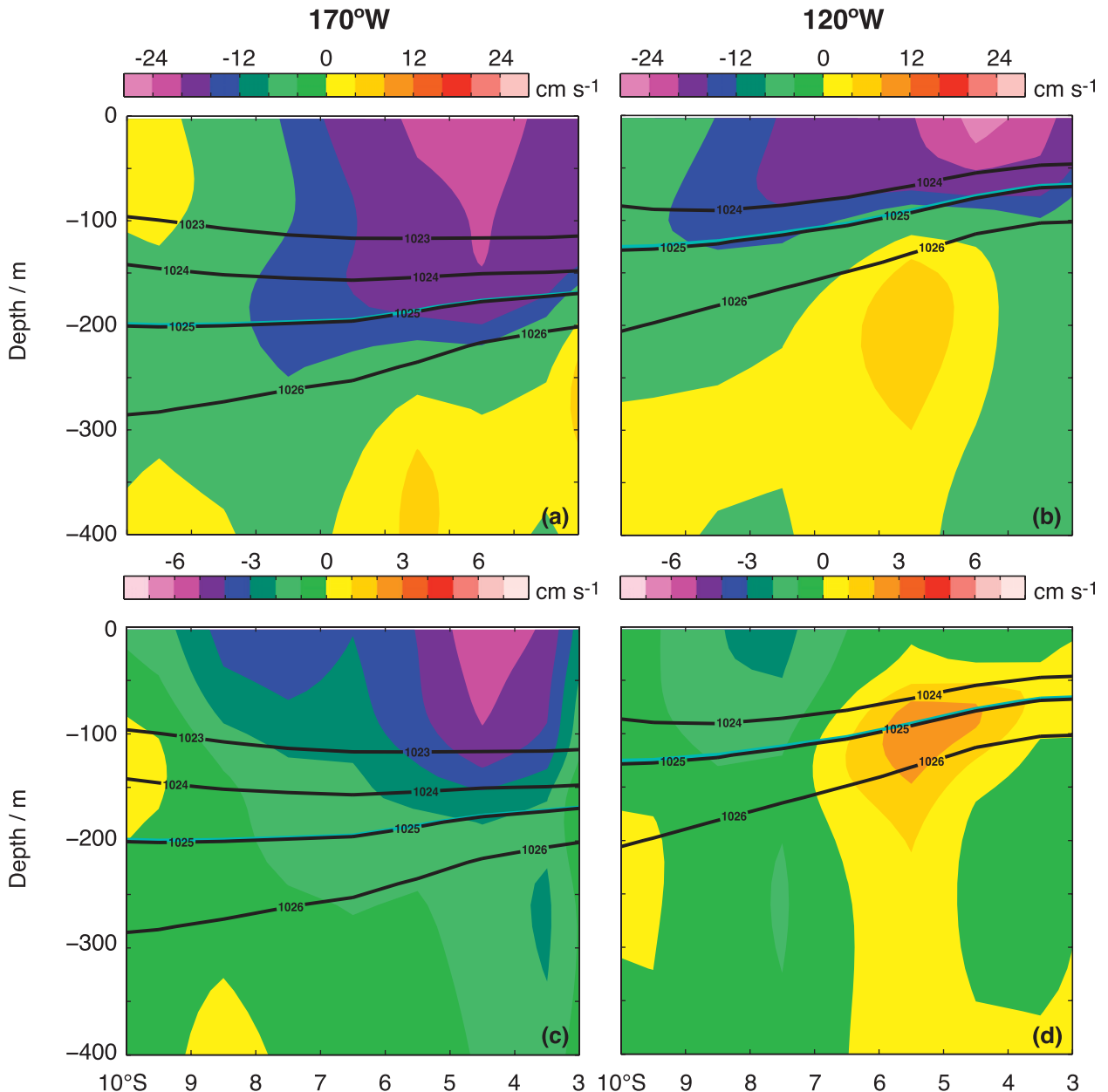


FIG. 4. Zonal geostrophic velocity u_g in the interior at (a) 170°W and (b) 120°W averaged from 2004 to 2011; (c),(d) the u_g anomaly for La Niña events. The black lines correspond to 2004–11 mean density contours (kg m^{-3}). The blue line corresponds to the 2004–11 mean steric anomaly surface $306 \times 10^{-8} \text{ m}^3 \text{ kg}^{-1}$.

(Fig. 3b). The increase in the northward flow is largest ($>0.01 \text{ m s}^{-1}$) in the western part of the interior, west of 160°W . The opposite tendencies are seen for El Niño episodes and hereafter for all La Niña/El Niño comparisons.

The 2004–11 mean zonal geostrophic velocity is shown in Figs. 4a and 4b along two meridional sections extending from 10° to 3°S at 170°W and at 120°W (black lines in Fig. 1). Above the 1026 kg m^{-3} density surface,

the zonal geostrophic velocity is westward ($u_g < 0$) at both 170° and 120°W , with the strongest flow north of 8°S indicating a core of the South Equatorial Current. The amplitude of the zonal geostrophic velocity within the SEC is in good agreement with observations by Kessler et al. (2003). The core of the SEC thins from 170° to 120°W as the pycnocline shoals to the east. Eastward flow at 5°S , 170°W , 400 m and at 5°S , 120°W , 200 m is indicative of the Southern Subsurface Countercurrent

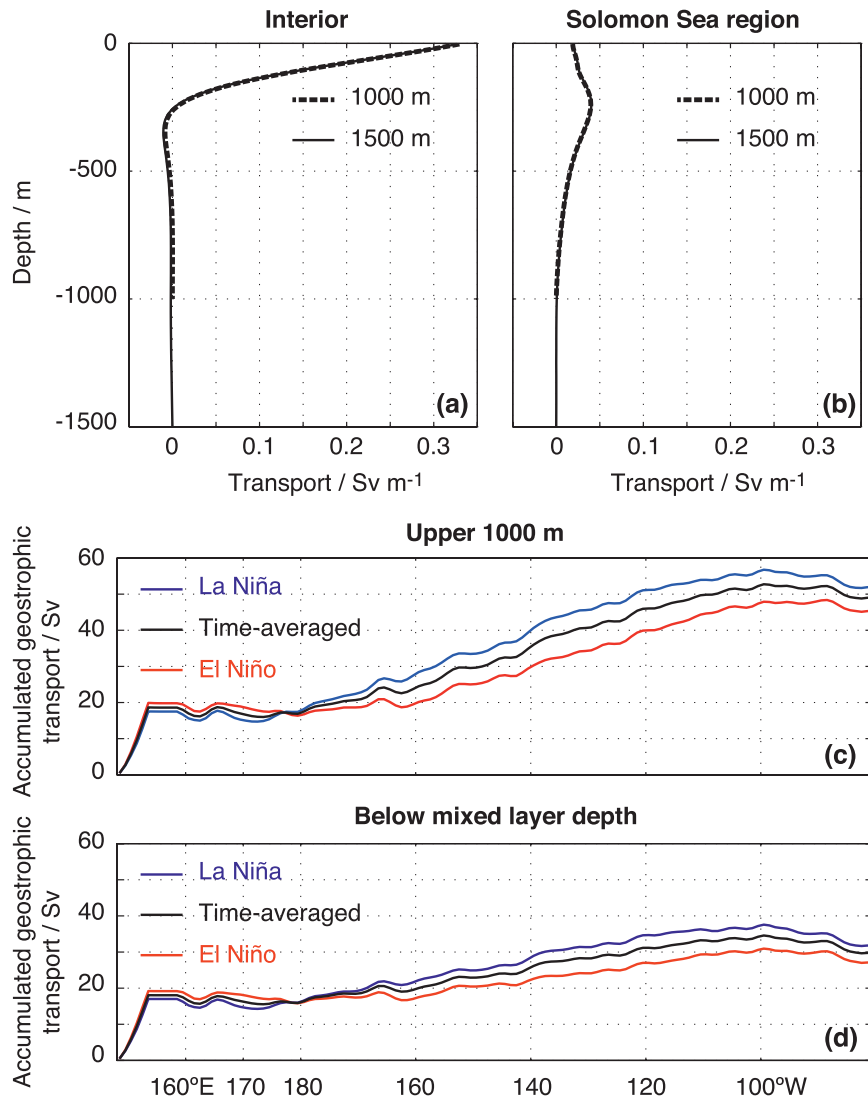


FIG. 5. Geostrophic transport per unit depth computed using a level of no motion at 1000 m (dashed line) and 1500 m (continuous line) in the (a) interior and (b) Solomon Sea region. Geostrophic transport accumulated from the coast of New Guinea eastward at 7.5°S (c) for the upper 1000 m averaged from 2004 to 2011 and (d) below the mixed layer depth (black) and for La Niña (blue) and El Niño (red) events of 2004–11.

(Tsuchiya 1981; McCreary et al. 2002). During La Niña events, the SEC strengthens (Figs. 4c,d), more so at 170°W than at 120°W.

In the ocean interior the mean meridional geostrophic transport at 7.5°S [$(V_g)_{\text{Interior}}$] is 31.7 ± 5.4 Sv equatorward (Figs. 5c and 12). Of this amount, 13.0 ± 4.4 Sv is below the mixed layer, as defined by a threshold temperature difference of 0.5°C (Fig. 5d). Here and for remaining transport calculations, reported uncertainties represent one standard deviation of the annual mean values. Our estimate of interior transport below the mixed layer is consistent with that reported

by Johnson and McPhaden (1999) for the 1967 to 1998 period. Northward transport below the mixed layer is apportioned as 6.5 ± 1.0 Sv in the density range of eastern South Pacific Subtropical Mode Water ($\sigma_\theta = 24.5\text{--}25.8$) (Sato and Suga 2009) with 9.9 ± 3.0 Sv above $\sigma_\theta = 24.5$ and -3.4 ± 1.1 Sv below $\sigma_\theta = 25.8$.

Relative to the 2004–11 mean, the $(V_g)_{\text{Interior}}$ anomalies exhibit an ENSO signature characterized by an increase during La Niña and a decrease during El Niño (Figs. 5c and 6a). The correlation coefficient between $(V_g)_{\text{Interior}}$ and the Niño-3.4 index is -0.9 for the 1-yr smoothed time series (Fig. 6b).

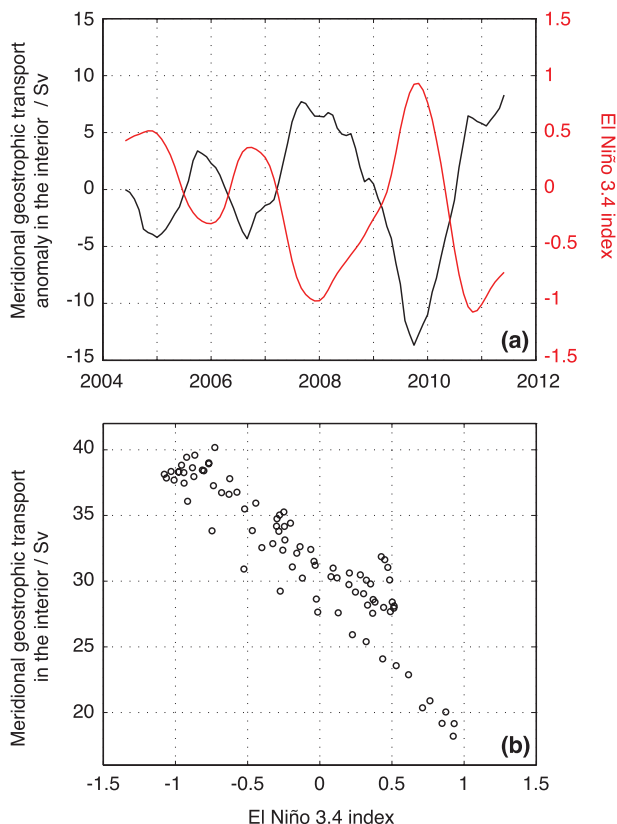


FIG. 6. (a) Time series of the geostrophic transport anomaly in the interior at 7.5°S and the Niño-3.4 index for monthly values from 2004 to 2011. (b) Scatterplot of the geostrophic transport in the interior at 7.5°S vs the Niño-3.4 index for monthly values of 2004–11.

2) THE SOLOMON SEA REGION

The meridional geostrophic velocity at 7.5°S in the Solomon Sea region averaged for 2004–11 is shown in Fig. 7a. Again we use a level of no motion at 1000 m since geostrophic transport estimates are similar for the 1000-m and 1500-m levels of no motion (Fig. 5b). The velocity estimates presented here are consistent with a finer grid constructed using 99 neighboring points instead of 300 in the least squares fit. West of the Solomon Islands the geostrophic velocity is oriented equatorward ($v_g > 0$), consistent with a deepening of the pycnocline from east to west. The northward flow that is the source of the NGCU is evident, with strong ($v_g > 0.02 \text{ m s}^{-1}$) meridional geostrophic velocity above 600 m. During La Niña events of the 2004–11 period this flow weakens, more so in the upper 200 m, and during El Niño it strengthens (Fig. 7b). On the eastern side of the Solomon Islands, the southward and the northward flows correspond to a recirculation of the SEC as the current hits the north–south elongated Solomon Islands chain

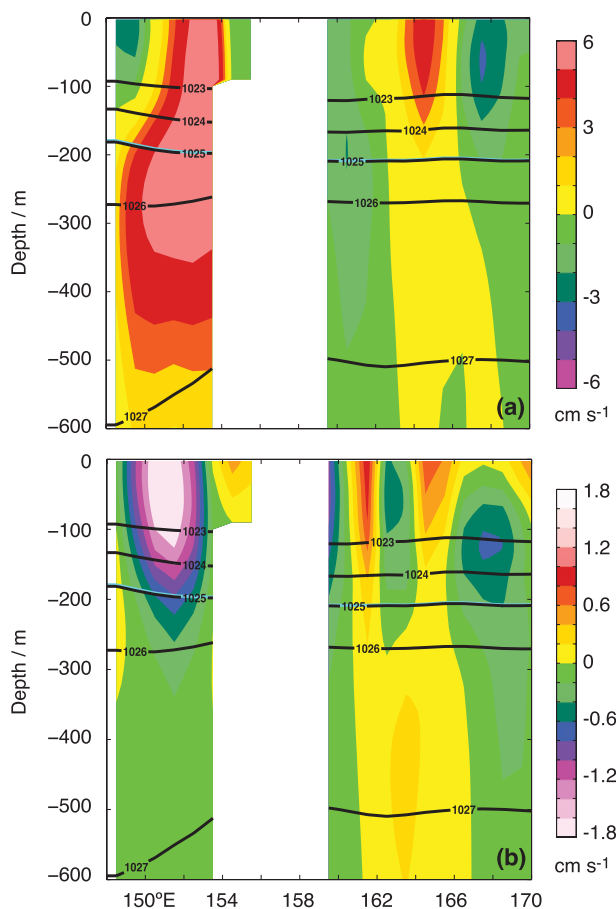


FIG. 7. Meridional geostrophic velocity v_g in the Solomon Sea region at 7.5°S (a) averaged from 2004 to 2011 and (b) the v_g anomaly for La Niña events. The black lines correspond to 2004–11 mean density contours (kg m^{-3}). The blue line corresponds to the 2004–11 mean steric anomaly surface $306 \times 10^{-8} \text{ m}^3 \text{ kg}^{-1}$.

(section 3a). During La Niña events the increased SEC is accompanied by a strengthening of the northward and southward currents on the eastern side of the Solomon Islands. The reverse occurs during El Niño.

The geostrophic transport in the Solomon Sea region is equatorward, as it is in the ocean interior. The 2004–11 mean geostrophic transport at 7.5°S in the Solomon Sea region [$(V_g)_{\text{Solomon}}$] is $17.2 \pm 2.0 \text{ Sv}$, half of the ocean interior (Fig. 12). West of the Solomon Islands the 2004–11 mean geostrophic transport is $18.7 \pm 1.4 \text{ Sv}$. In the upper 300 m the Argo estimate is consistent with ship-mounted ADCP measurements by Cravatte et al. (2011) collected between 1997 and 2007. Argo profiles indicate a mean northward geostrophic transport 2.8 Sv greater than from Spray glider relative geostrophic velocity estimates by Davis et al. (2012) above 700 m but 6.1 Sv lower than from hydrographic measurements by Sokolov and Rintoul (2000) within the 0–1000-m range.

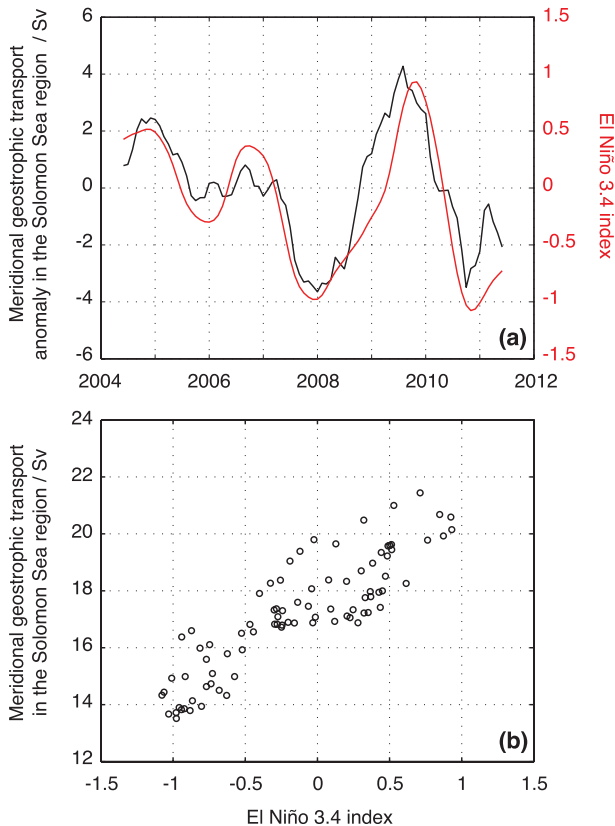


FIG. 8. (a) Time series of the geostrophic transport anomaly in the Solomon Sea region at 7.5°S and the Niño-3.4 index for monthly values 2004–11. (b) Scatterplot of the geostrophic transport in the Solomon Sea region at 7.5°S vs the Niño-3.4 index for monthly values from 2004 to 2011.

In the Solomon Sea region the geostrophic transport anomalies relative to the 2004–11 mean show a strong ENSO signature with a decrease during La Niña and an increase during El Niño (Figs. 5c and 8a). The correlation coefficient between $(V_g)_{\text{Solomon}}$ and the Niño-3.4 index is 0.9 for the 1-yr smoothed time series (Fig. 8b). The interannual variability of the geostrophic transport in the Solomon Sea region is half of the ocean interior variability (Figs. 8a and 6a), but has opposite phasing relative to ENSO. Therefore, the time variability in the basinwide geostrophic transport at 7.5°S (V_g) resembles the transport in the ocean interior and is characterized by an increase during La Niña and a decrease during El Niño. The ENSO signature seen in $(V_g)_{\text{Solomon}}$ is in agreement with the numerical predictions of Lübbecke et al. (2007), who showed that the time variability of western South Pacific geostrophic transport is related to a shift in latitude of the SEC bifurcation. During La Niña events, the poleward extent of the tropical gyre retracts and the SEC bifurcation moves equatorward. This generates a decreased flow in the northward

turning branch of the SEC and a weakening of the NGCU.

The counteracting tendency of the transport in the Solomon Sea region and the ocean interior seen in the Argo profiles is in agreement with altimetric height anomalies for the same time period (Figs. 9a,b). During La Niña events the anomalous slopes of altimetric height along 7.5°S indicate a strengthening of the geostrophic transport in the interior and a weakening of the transport in the Solomon Sea region. This tendency is explained as a combined effect of two anticorrelated forcings: the off-equatorial wind stress curl in the western Pacific and the near-equatorial zonal wind stress in the interior Pacific. During La Niña events the wind stress curl is less negative in the western Pacific (Fig. 10). This leads to a sea level rise in the western Pacific, an increase in the geostrophic transport in the interior, and a decrease in the Solomon Sea region. In addition, the equatorial easterly wind perturbation increases the upward slope of sea level toward the west. This generates a strengthening of the geostrophic transport in the interior. The counteracting tendency of the geostrophic transport in the Solomon Sea region and the interior, and the larger variability of the geostrophic transport in the interior than in the Solomon Sea, are in agreement with the numerical predictions of Lee and Fukumori (2003). Numerical simulations by Capotondi et al. (2005) indicate that westward propagating Rossby waves excited by anomalous Ekman pumping generate opposite density anomalies and, hence, anticorrelated geostrophic transport in the Solomon Sea region and the ocean interior. The interannual anomalies in surface geostrophic transport using Argo at 7.5°S are lower than those from the Archiving, Validation, and Interpretation of Satellite Oceanographic (AVISO) data along 7.5°S but similar to AVISO values averaged for 5°–10°S (Figs. 9b–d). This is consistent with the objectively mapped gridded Argo being a smoother representation than the AVISO altimetric product. The small discrepancies between Argo and AVISO in the transport variability for the Solomon Sea region are induced by the loss of variance from undersampling in the Solomon Sea objective mapping. The regression slope of AVISO interior transport at 7.5°S onto the Niño-3.4 index for the 8-yr record agrees within 95% confidence with the 1993–2011 record (not shown). This provides additional evidence that the 8-yr Argo record captures the patterns of ENSO variability.

West of the Solomon Islands the geostrophic transport is decreased during La Niña and increased during El Niño, as also indicated by Spray glider measurements collected between 2007 and 2011 (Davis et al. 2012). The peak to trough amplitude of the geostrophic transport computed in the upper 700 m from the gliders is 15 Sv,

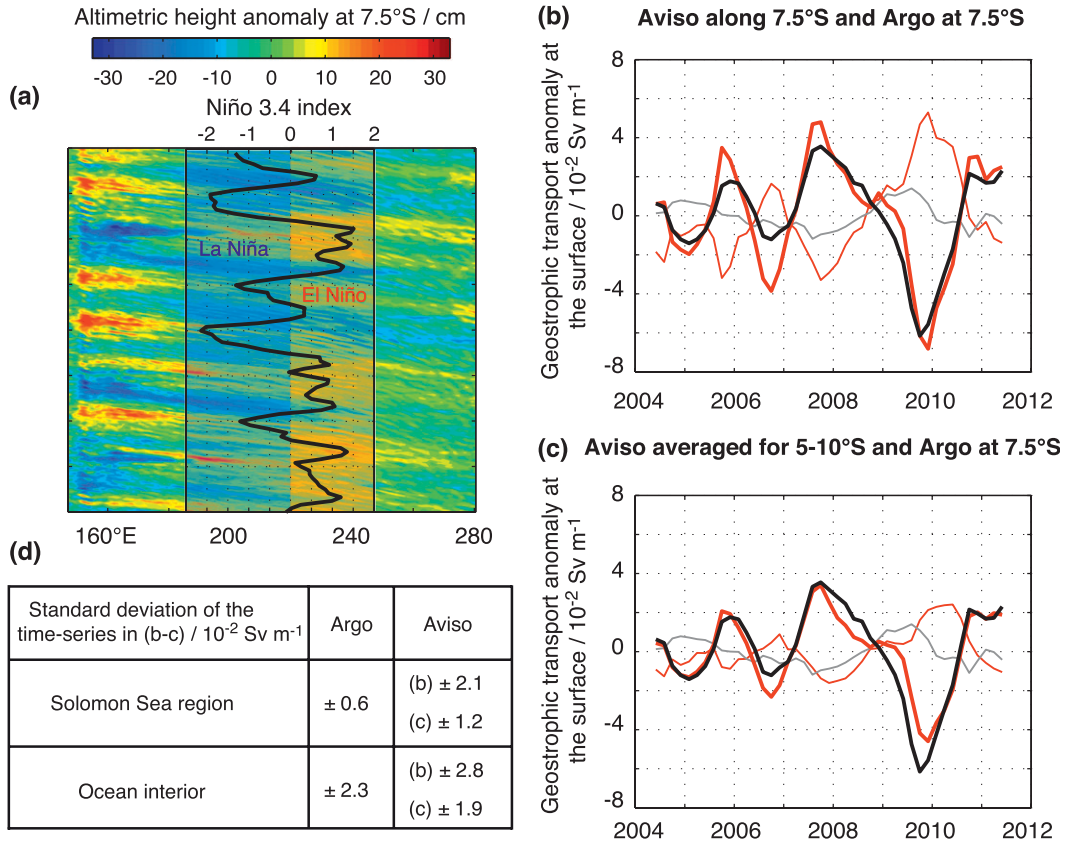


FIG. 9. (a) Altimetric height anomaly at 7.5°S from AVISO for weekly values 2004 to 2011 with the corresponding Niño-3.4 index. (b) Time series of the geostrophic transport anomaly at the surface computed using AVISO along 7.5°S (red) and Argo at 7.5°S (black) for the ocean interior (thick lines) and the Solomon Sea region (thin lines) for monthly values from 2004 to 2011. (c) Time series of the geostrophic transport anomaly at the surface computed using AVISO for 5°–10°S (red) and Argo at 7.5°S (black) for the ocean interior (thick lines) and the Solomon Sea region (thin lines) for monthly values from 2004 to 2011. (d) Standard deviation of the time series for Argo and AVISO in (b) and (c).

which is 13.5 Sv higher than Argo and 9.1 Sv higher than the AVISO variability adjusted to the 0–700-m depth range using Argo between 2007 and 2012. This discrepancy could result from 1) the snapshot sampling from the gliders versus the annual mean from Argo and 2) the limited number of roundtrips across the Solomon Sea for

each year. Ongoing glider sampling in the Solomon Sea will provide additional geostrophic transport estimates.

b. Ekman and total transport

The 2004–11 mean basinwide Ekman transport at 7.5°S (V_{EK}) is -39.6 ± 4.1 Sv poleward using ECMWF and

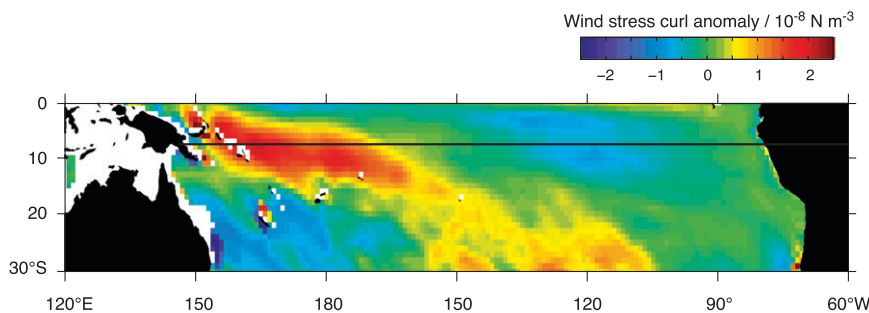


FIG. 10. Wind stress curl anomaly for La Niña events from 2004 to 2011 in the tropical South Pacific Ocean. The continuous black line indicates 7.5°S.

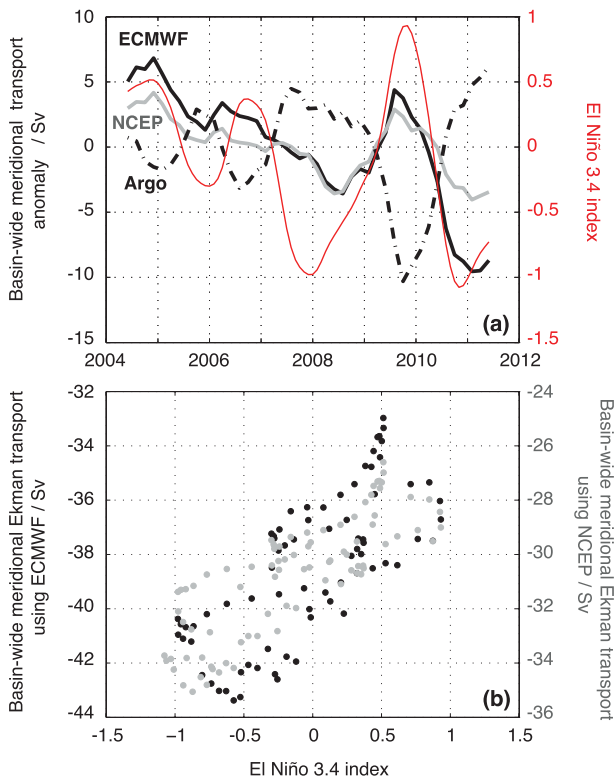


FIG. 11. (a) Time series of the basinwide Ekman transport and geostrophic transport anomalies at 7.5°S and the Niño-3.4 index for monthly values from 2004 to 2011. (b) Scatterplot of the basinwide Ekman transport at 7.5°S vs the Niño-3.4 index for monthly values from 2004 to 2011.

-30.7 ± 2.1 Sv using NCEP (Fig. 12). The corresponding Ekman transport computed from the QuikSCAT product (<http://coaps.fsu.edu/>) falls halfway between the NCEP and ECMWF estimates for the common time period. Our estimate of the 2004–11 mean basinwide Ekman transport at 7.5°S is therefore the midvalue of -35.2 ± 3.0 Sv between the NCEP and ECMWF rates.

The basinwide Ekman transport anomalies relative to the 2004–11 mean show an ENSO signature with an increase during La Niña and a decrease during El Niño (Fig. 11a). The correlation coefficient between the Ekman transport and the Niño-3.4 index is 0.8 for both ECMWF and NCEP 1-yr smoothed time series (Fig. 11b). The interannual variability of the Ekman transport is less than the geostrophic transport but has opposite phasing relative to ENSO such that anomalously strong poleward Ekman transport is accompanied by anomalously strong equatorward geostrophic transport (Figs. 11a,c). The increased Ekman transport during La Niña events is consistent with a cooling of the SST in the central and eastern equatorial Pacific, which leads to a strengthening of the trade winds over the tropical Pacific. The pycnocline shoals toward the east as the trade winds

strengthen, which leads to an increase in the meridional geostrophic transport. This is consistent with previous observations by McPhaden and Zhang (2002).

c. Volume transport in the ITF

The Indonesian Seas provide a conduit for very warm water to pass between the Pacific and Indian Oceans. In the Northern Hemisphere, the geostrophic transport and the Ekman transport within the STC have similar magnitudes and opposite signs, which implies a net volume transport close to zero. The Indonesian Seas are fed by southern Pacific Ocean waters, which either flow directly through the southernmost passages of the Indonesian Seas or recirculate in the North Pacific Ocean via the North Equatorial Countercurrent and the North Equatorial Current before entering the ITF through the northern passages. Assuming conservation of mass within a box representing the 0 to 1000-m depth range of the Pacific Ocean north of 7.5°S , we compute the time-varying ITF volume transport:

$$V_{\text{ITF}} = -(V_g + V_{\text{Ek}} + W_{1000}), \quad (1)$$

where $W_{1000} = \int_A w(z=1000) dA$ is the vertical transport at 1000 m over all of the Pacific north of 7.5°S ; A is the surface area of the Pacific Ocean north of 7.5°S ,

$$w(z) = \frac{\partial \rho / \partial t}{\partial \bar{\rho} / \partial z}$$

is the time-varying vertical velocity, ρ is the potential density, and the overbar indicates an 8-yr time average. The 2004–11 mean W_{1000} is 0.4 ± 3.5 Sv. Positive transport is defined to be into the box. The magnitude of evaporation minus precipitation of 0.1 Sv using ECMWF and 0.08 Sv using NCEP within the box are small compared to basinwide geostrophic and Ekman transport. The interannual variability of evaporation minus precipitation north of 7.5°S of 0.1 Sv using ECMWF and 0.07 Sv using NCEP are small compared to the basinwide geostrophic and Ekman transport and the vertical transport north of 7.5°S . The contribution of the evaporation minus precipitation to the conservation of mass at 7.5°S is hence not considered in our analysis. In addition, the contribution of the Bering Strait transport to the conservation of mass was ignored in our analysis.

For 2004–11 the mean V_{ITF} is -18.6 ± 4.7 Sv using NCEP and -9.7 ± 5.0 Sv using ECMWF for the Ekman transport (Fig. 12). The midvalue of -14.2 ± 4.7 Sv between the V_{ITF} values computed using NCEP and ECMWF is consistent with the Simple Ocean Data Assimilation model (SODA) simulations by Potemra and Schneider (2007) for the 1993–98 time period and with observations by Sprintall et al. (2009) from 2004 to 2006.

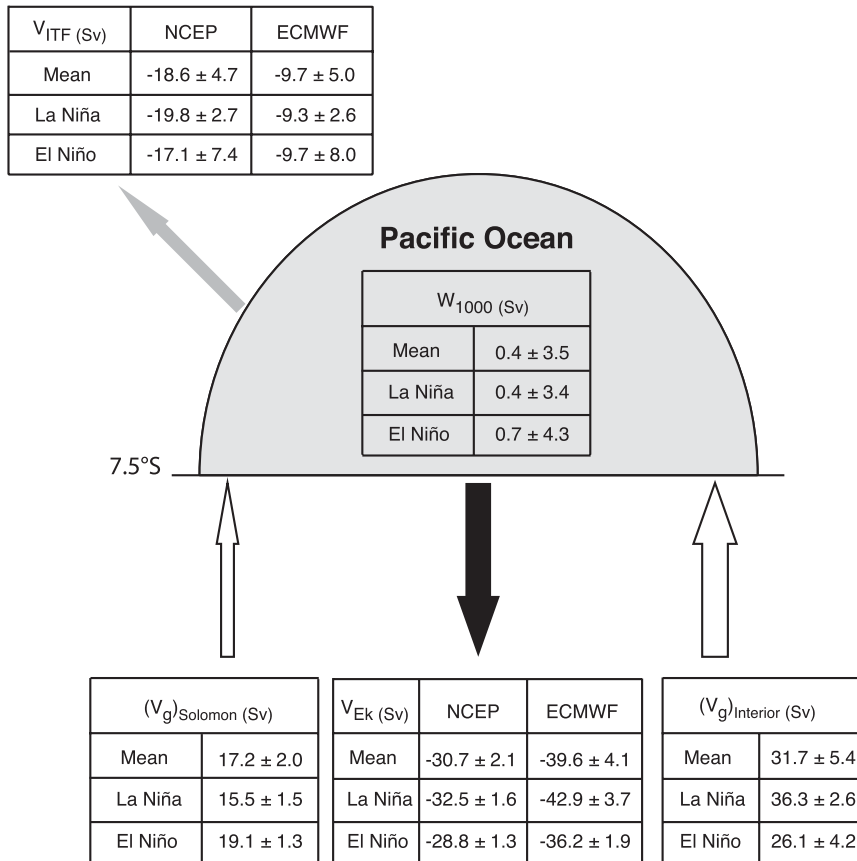


FIG. 12. Schematic of the geostrophic transport in the Solomon Sea region [$(V_g)_{Solomon}$], geostrophic transport in the interior Pacific [$(V_g)_{Interior}$], Ekman transport across 7.5°S (V_{Ek}), vertical transport at 1000 m over all the Pacific north of 7.5°S (W_{1000}), and the Indonesian Throughflow (V_{ITF}) averaged from 2004 to 2011 and for La Niña and El Niño events of 2004–11.

Consistency of the V_{ITF} midvalue with observations by Sprintall et al. suggests an uncertainty of a few Sverdrups.

Relative to the 2004–11 mean, the anomalies in the residual of the geostrophic transport and the Ekman transport at 7.5°S show an ENSO signature generally characterized by an increase during La Niña and a decrease during El Niño (Fig. 13a). The W_{1000} anomalies appear to exhibit a 2-yr periodicity rather than an ENSO correlation (Fig. 13b). The interannual variability of W_{1000} is twice the residual of the geostrophic transport and the Ekman transport. The V_{ITF} variability resembles the vertical transport at 1000 m and is affected by the residual of the geostrophic transport and the Ekman transport within the STC (Figs. 13a–c).

4. Heat budget in the Pacific Ocean north of 7.5°S

a. Mass-balanced cells

To estimate the heat budget, we consider the flow across 7.5°S to include three mass-balanced components. These

are (i) geostrophic transport in the surface layer that recirculates in the surface layer as Ekman transport, (ii) geostrophic transport in the thermocline that upwells and returns as Ekman transport, and (iii) geostrophic transport in the thermocline that feeds the ITF [Eq. (1)]. This equation also has a contribution from the vertical velocity at 1000 m (W_{1000}), averaged over all of the Pacific north of 7.5°S . The mean mass-balanced components (i) and (ii) are presented in Fig. 14.

The volume transport (i) within the surface recirculation cell (SRC) is

$$V_{g-ML} = -V_{Ek-SRC}, \quad (2)$$

where V_{g-ML} is the meridional geostrophic transport in the mixed layer (ML) and V_{Ek-SRC} is the meridional Ekman transport in the SRC at 7.5°S . The 2004–11 mean V_{g-ML} is 19.2 ± 0.9 Sv.

The volume transport (ii) within the meridional overturning circulation (MOC) is

field. Mooring observations by Sprintall et al. (2009) provide in situ observations for 2004–06. The Sprintall et al. T_{ITF} value of 17.9°C is used in Eq. (7) with an assumption that the variations in T_{ITF} are small from 2006 to 2011.

The vertical advection of heat north of 7.5°S is

$$\text{Adv}_z = \rho_0 c_p (T_{1000} - T_{g-\text{Th}}) W_{1000}, \quad (8)$$

where T_{1000} is the temperature of W_{1000} . The 2004–11 mean T_{1000} is $4.3 \pm 0.3^\circ\text{C}$.

The heat storage north of 7.5°S is

$$S = \int_A \int_{1000}^0 \rho_0 c_p \frac{\partial T}{\partial t} dz dA, \quad (9)$$

where T is the temperature. Using a vertical diffusivity coefficient of $10^{-4} \text{ m}^2 \text{ s}^{-1}$ representative of the ocean interior (Munk and Wunsch 1998), the vertical diffusion rate computed at 1000 m depth north of 7.5°S is negligible compared to the terms in Eqs. (5)–(9). The contribution of the vertical diffusion to the heat budget is hence not considered here. The eddy contribution to the mean heat transport at 7.5°S, based on monthly values of velocity and temperature, is 0.004 PW and is negligible compared to mean flow components. The contribution of eddy heat transport in the time-varying balance was also found to be small by Cheng et al. (2007) and is not considered in the heat budget here.

The total heat transport into the enclosed region is the sum of the three components:

$$H = H_{\text{SRC}} + H_{\text{MOC}} + H_{\text{ITF}}. \quad (10)$$

The air–sea heat flux north of 7.5°S is

$$Q = \int_A Q_l + Q_s + Q_{\text{lw}} + Q_{\text{sw}} dA, \quad (11)$$

where Q_l is the latent heat of evaporation, Q_s is the sensible heat flux induced by the temperature difference between the ocean and the atmosphere, Q_{lw} is the net longwave radiative flux, and Q_{sw} is the net shortwave radiative flux.

Finally, the heat balance is expressed as

$$S = H + \text{Adv}_z + Q. \quad (12)$$

The total heat transport computed from Eq. (10) is negative, indicative of a heat transport out of the region north of 7.5°S (Table 1). The heat transport in the MOC is the dominant term in the mean heat export from the equatorial Pacific. The heat transport in the

TABLE 1. Heat transport in the SRC (H_{SRC}), MOC (H_{MOC}), and in waters feeding the ITF (H_{ITF}), total heat transport into the region north of 7.5°S (H), heat storage above 150 m (S_{up}), below 150 m (S_{low}), and in the upper 1000 m (S), vertical advection of heat (Adv_z), air–sea flux (Q), and residual of the oceanic heat transport, heat storage, vertical advection of heat, and air–sea flux ($H - S + \text{Adv}_z + Q$) in the region north of 7.5°S averaged from 2004 to 2011 using NCEP and ECMWF.

Heat budget terms (PW)	NCEP	ECMWF
H_{SRC}	$+0.06 \pm 0.01$	$+0.05 \pm 0.01$
H_{MOC}	-0.37 ± 0.05	-0.65 ± 0.08
H_{ITF}	$+0.04 \pm 0.03$	$+0.03 \pm 0.02$
H	-0.27 ± 0.07	-0.57 ± 0.10
S_{up}		-0.02 ± 0.25
S_{low}		-0.01 ± 0.18
S		-0.03 ± 0.14
Adv_z		-0.01 ± 0.16
Q	$+0.89 \pm 0.20$	$+1.16 \pm 0.31$
$H - S + \text{Adv}_z + Q$	$+0.64 \pm 0.16$	$+0.61 \pm 0.26$

SRC and the heat transport in the ITF are small. The region north of 7.5°S loses heat in the MOC ($H_{\text{MOC}} < 0$) because exported waters are warmer than imported waters below the mixed layer. A small amount of heat is gained in the SRC ($H_{\text{SRC}} > 0$) and the ITF ($H_{\text{ITF}} > 0$) since exported waters in the SRC are cooler than imported waters in the mixed layer, and exported waters feeding the ITF are cooler than imported below the mixed layer. Since individual water parcels cannot be tracked through the equatorial region, the specific decomposition of section 4a is somewhat arbitrary, but nevertheless illustrative. The 2004–11 mean total heat transport is -0.62 ± 0.13 PW using ECMWF for the Ekman transport and the volume transport in the ITF, and -0.29 ± 0.07 PW using NCEP (Table 1). Using the midpoint values of the Ekman transport consistent with QuikSCAT (section 3b) and the volume transport in the ITF consistent with observations and SODA simulations (section 4a), the residual of the total heat transport, heat storage, and vertical advection of heat is -0.40 ± 0.20 PW. The mean heat storage and vertical advection of heat are fairly minor compared to the heat transport (Table 1).

The air–sea flux (Q) north of 7.5°S computed from Eq. (11) is positive, which implies a heat gain by the ocean from the atmosphere. The 2004–11 mean air–sea heat flux computed using ECMWF and NCEP indicate an oceanic heat gain higher than justified by the heat transport (Table 1). The residual of the oceanic heat transport into the region north of 7.5°S, and the heat storage, vertical advection of heat, and air–sea flux in the region north of 7.5°S is 0.59 ± 0.27 PW using ECMWF to estimate Ekman transport and 0.67 ± 0.19 PW using NCEP

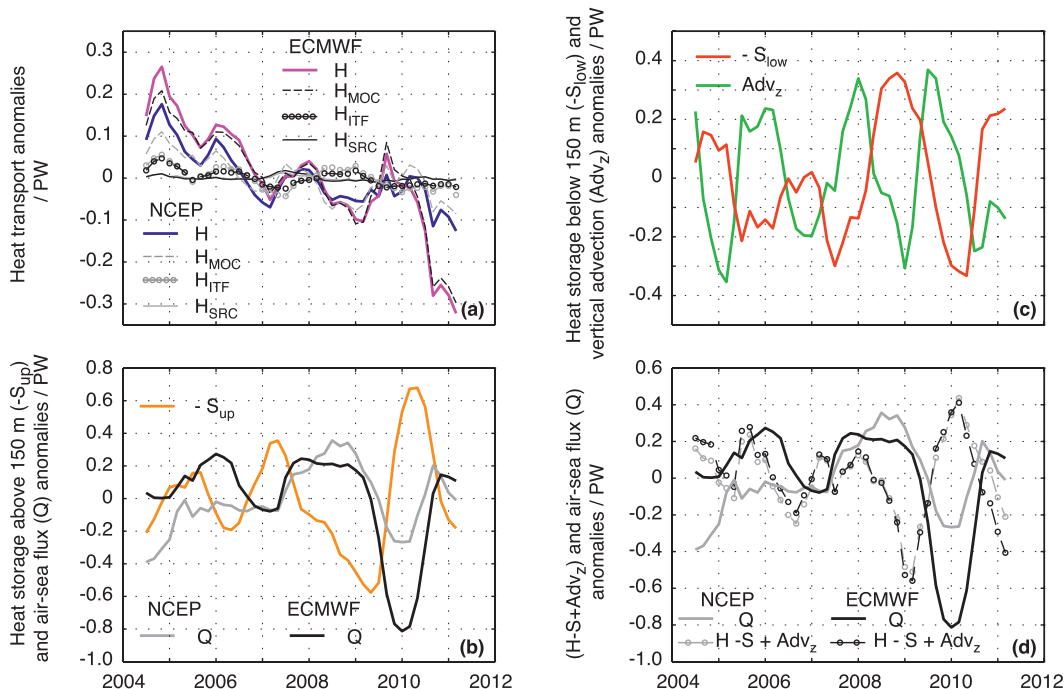


FIG. 15. (a) Time series of the heat transport in the SRC (H_{SRC}), MOC (H_{MOC}), and in waters feeding the ITF (H_{ITF}), and total heat transport (H) anomalies into the region north of 7.5°S for monthly values from 2004 to 2011 using NCEP and ECMWF. (b) Time series of the heat storage above 150 m ($-S_{\text{up}}$) and air-sea flux (Q) anomalies in the region north of 7.5°S for monthly values from 2004 to 2011 using NCEP and ECMWF. (c) Time series of the heat storage below 150 m ($-S_{\text{low}}$) and vertical advection of heat (Adv_z) anomalies in the region north of 7.5°S for monthly values from 2004 to 2011. (d) Time series of the air-sea flux (Q) and residual of the oceanic heat transport, heat storage, and vertical advection of heat ($H - S + \text{Adv}_z$) anomalies in the region north of 7.5°S for monthly values from 2004 to 2011 using NCEP and ECMWF.

(Table 1). This residual, possibly attributable to systematic errors in the reanalysis air-sea fluxes, amounts to 7.4 W m^{-2} for ECMWF and 8.4 W m^{-2} for NCEP, consistent with the findings of Grist and Josey (2003). That is, the mean air-sea heat flux for this region in the NOCS climatology 1.1a, which is adjusted to be consistent with ocean heat transport, is 0.52 PW for the period 1980–93. If also adjusted to the 2004–11 time period using the ECMWF and NCEP time series, this is $0.45 \pm 0.09 \text{ PW}$. Thus the air-sea flux in the NOCS 1.1a climatology balances, within errors, the mean residual of our estimated heat transport and storage.

The interannual variability of the heat transport into the region north of 7.5°S is less than that of heat storage, vertical advection of heat, and air-sea flux in that region (Figs. 15a–d). The anomalies of the heat storage in the upper 150 m ($-S_{\text{up}}$) appear roughly in balance with the air-sea flux north of 7.5°S (Fig. 15b). The anomalies of the heat storage below 150 m ($-S_{\text{low}}$) appears to exhibit a 2-yr periodicity generally in opposite phasing with the vertical advection of heat north of 7.5°S (Fig. 15c), indicating that these two terms tend to balance one

another. The residual of heat transport, storage, and vertical advection of heat exhibits large positive anomalies at the end of 2004 and 2009 and large negative anomalies in 2008 and at the beginning of 2009 (Fig. 15d). These larger anomalies in the residual appear in balance with the air-sea flux products. Clearly a longer record is needed to assess the time-varying heat budget.

5. Summary and conclusions

In this study, our first objective has been to examine the time variability of the volume transport of the subtropical cell (STC) for 2004–11 using gridded Argo temperature and salinity profiles and atmospheric reanalysis products. The geostrophic transport in the ocean interior shows a strong ENSO signature characterized by an increase during La Niña and a decrease during El Niño. The interannual variations of the geostrophic transport in the Solomon Sea region are anticorrelated with, and half the size of, changes in the ocean interior. These two results are in agreement with the

simulations by Lohmann and Latif (2005) and Lee and Fukumori (2003). The variability of the basinwide geostrophic transport resembles the transport in the ocean interior. The basinwide geostrophic transport and Ekman transport anomalies are about 4 Sv per unit of the Niño-3.4 index. Since the poleward Ekman transport is correlated with the equatorward geostrophic transport, the strength of the STC, and hence the equatorial upwelling, increases during La Niña and decreases during El Niño. Geostrophic transport estimates are accurately determined in the ocean interior but are more uncertain in the Solomon Sea region. Limitations lie primarily in the uncertainty introduced by coarse float sampling. Ongoing hydrographic and glider sampling and additional Argo float deployments will provide better spatial resolution in the Solomon Sea region and improved accuracy of the transport estimates.

Our results indicate that the southern sources for the equatorial thermocline have a transit time from the subduction region to the equator of 2 yr, much shorter than from the northern sources. This suggests faster transmission of subtropical anomalies to the tropics in the southern STC. The extent to which the Pacific decadal oscillation and the South Pacific oceanic variability can impact ENSO variability are issues that will require an extended Argo data record.

Another objective of this work has been to investigate the time variability of the Indonesian Throughflow (Fig. 13). Since the net equatorward transport in the North Pacific STC is limited by the closed geometry of that basin, the ITF was estimated as the residual of the net transport in the South Pacific STC and the vertical transport at 1000 m over all of the Pacific north of 7.5°S. Although not measured directly, our mean ITF estimate is in agreement with local observations in the Indonesian Seas. At interannual time scales, the net transport in the South Pacific STC shows an ENSO signature characterized by an increase during La Niña, as noted above. The vertical volume transport anomalies at 1000 m exhibit a periodicity that is not obviously related to ENSO. The ITF variability is affected by the net transport in the South Pacific STC and the vertical transport at 1000 m. The factors responsible for the low frequency variability seen in the vertical transport at 1000 m are a subject for further exploration.

Our final objective has been to quantify the ocean heat budget in the Pacific Ocean north of 7.5°S. Air–sea flux computed using NCEP and ECMWF analyses indicate an oceanic heat gain from the atmosphere that is much larger than the heat transport out of the region by the ocean circulation. The smaller heat gain in the NOCS climatology version 1.1a (adjusted for consistency with earlier estimates of ocean heat transport) is

consistent with the present analysis. In the time-varying heat budget, the heat storage above 150 m and the air–sea heat exchange tend to balance one another. The anomalies in the heat transport induced by the STC are smaller than the heat storage and the vertical advection of heat. These results suggest that the STC plays a minor role (directly) in the interannual variability of the heat budget north of 7.5°S. However, the heat transport fluctuations in the meridional overturning circulation may still be important in conditioning the equatorial ocean by way of strengthening the existing El Niño/La Niña conditions on decadal time scales.

Acknowledgments. The Argo data used here were collected and are made freely available by the International Argo Program and by the national programs that contribute to it. The authors thank John Gilson, Megan Scanderbeg, and Lisa Lehmann for valuable suggestions. This work was supported by U.S. Argo through NOAA Grant NA17RJ1231 (SIO-JIMO), and by NOAA award NA10OAR4310139 and NASA Grant NNX08AI82G. The altimeter products were produced by Ssalto/Duacs and distributed by Aviso with support from the Centre National d'Etudes Spatiales (CNES).

REFERENCES

- Alexander, M. A., I. Bladé, M. Newman, J. R. Lanzante, N. Lau, and J. Scott, 2002: The atmospheric bridge: The influence of ENSO teleconnections on air–sea interactions over the global oceans. *J. Climate*, **15**, 2205–2231.
- Bentamy, A., K. B. Katsaros, A. M. Mestas-Nuñez, W. M. Drennan, E. B. Forde, and H. Roquet, 2003: Satellite estimates of wind speed and latent heat flux over the global oceans. *J. Climate*, **16**, 637–656.
- Berrisford, P., D. Dee, K. Fielding, M. Fuentes, P. Kallberg, S. Kobayashi, and S. Uppala, 2009: The ERA-Interim archive, version 1.0. ECMWF Tech. Rep., 16 pp.
- Brunke, M. A., Z. Wang, X. Zeng, M. Bosilovich, and C. Shie, 2011: An assessment of the uncertainties in ocean surface turbulent fluxes in 11 reanalysis, satellite-derived, and combined global datasets. *J. Climate*, **24**, 5469–5493.
- Capotondi, A., M. A. Alexander, C. Deser, and M. J. McPhaden, 2005: Anatomy and decadal evolution of the Pacific subtropical tropical cells (STCs). *J. Climate*, **18**, 3739–3758.
- Chelton, D. B., and M. H. Freilich, 2005: Scatterometer-based assessment of 10-m wind analyses from the operational ECMWF and NCEP numerical weather prediction models. *Mon. Wea. Rev.*, **133**, 409–429.
- , —, J. M. Sienkiewicz, and J. M. Von Ahn, 2006: On the use of QuikSCAT scatterometer measurements of surface winds for marine weather prediction. *Mon. Wea. Rev.*, **134**, 2055–2071.
- Cheng, W., M. J. McPhaden, D. Zhang, and E. J. Metzger, 2007: Recent changes in the Pacific subtropical cells inferred from an eddy-resolving ocean circulation model. *J. Phys. Oceanogr.*, **37**, 1340–1356.

- Cravatte, S., A. Ganachaud, Q. Duong, W. S. Kessler, G. Eldin, and P. Dutilleul, 2011: Observed circulation in the Solomon Sea from SADC data. *Prog. Oceanogr.*, **88**, 116–130.
- Davis, R. E., W. S. Kessler, and J. T. Sherman, 2012: Gliders measure western boundary current transport from the South Pacific to the equator. *J. Phys. Oceanogr.*, **42**, 2001–2013.
- Decker, M., M. A. Brunke, Z. Wang, K. Sakaguchi, X. Zeng, and M. G. Bosilovich, 2011: Evaluation of the reanalysis products from GSFC, NCEP, and ECMWF using flux tower observations. *J. Climate*, **25**, 1916–1944.
- Dee, D. P., and Coauthors, 2011: The ERA-Interim reanalysis: Configuration and performance of the data assimilation system. *Quart. J. Roy. Meteor. Soc.*, **137**, 553–597.
- Gordon, A. L., 2005: Oceanography of the Indonesian Seas and their throughflow. *Oceanography*, **18**, 14–27.
- Grist, J. P., and S. A. Josey, 2003: Inverse analysis adjustment of the SOC air–sea flux climatology using ocean heat transport constraints. *J. Climate*, **16**, 3274–3295.
- Gu, D., and S. G. H. Philander, 1997: Interdecadal climate fluctuations that depend on exchanges between the tropics and extratropics. *Science*, **275**, 805–807.
- Johnson, G. C., and M. J. McPhaden, 1999: Interior pycnocline flow from the subtropical to the equatorial Pacific Ocean. *J. Phys. Oceanogr.*, **29**, 3073–3089.
- , and —, 2001: Equatorial Pacific Ocean horizontal velocity, divergence, and upwelling. *J. Phys. Oceanogr.*, **31**, 839–849.
- Kalnay, E., and Coauthors, 1996: The NCEP/NCAR 40-Year Reanalysis Project. *Bull. Amer. Meteor. Soc.*, **77**, 437–471.
- Kessler, W., G. Johnson, and D. Moore, 2003: Sverdrup and nonlinear dynamics of the Pacific equatorial currents. *J. Phys. Oceanogr.*, **33**, 994–1008.
- Kleeman, R., J. P. McCreary, and B. A. Klinger, 1999: A mechanism for generating ENSO decadal variability. *Geophys. Res. Lett.*, **26**, 1743–1746.
- Klinger, B. A., J. P. McCreary, and R. Kleeman, 2002: The relationship between oscillating subtropical wind stress and equatorial temperature. *J. Phys. Oceanogr.*, **32**, 1507–1521.
- Kobayashi, T., and S. Minato, 2005: What observation scheme should we use for profiling floats to achieve the Argo goal for salinity measurement accuracy? Suggestions from software calibration. *J. Atmos. Oceanic Technol.*, **22**, 1588–1601.
- Kumar, B. P., J. Vialard, M. Lengaigne, V. S. N. Murty, and M. J. McPhaden, 2012: TropFlux: Air–sea fluxes for the global tropical oceans, description and evaluation. *Climate Dyn.*, **38**, 1521–1543.
- Large, W. G., J. C. McWilliams, and S. C. Doney, 1994: Oceanic vertical mixing: A review and a model with a nonlocal boundary layer parameterization. *Rev. Geophys.*, **32**, 363–403.
- Lee, T., and I. Fukumori, 2003: Interannual-to-decadal variations of tropical–subtropical exchange in the Pacific Ocean: Boundary versus interior pycnocline transports. *J. Phys. Oceanogr.*, **16**, 4022–4042.
- Lohmann, K., and M. Latif, 2005: Tropical Pacific decadal variability and the subtropical–tropical cells. *J. Climate*, **18**, 5163–5178.
- Lu, P., J. McCreary, and B. Klinger, 1998: Meridional circulation cells and the source waters of the Pacific Equatorial Undercurrent. *J. Phys. Oceanogr.*, **28**, 62–84.
- Lübbecke, J. F., C. W. Böning, and A. Biastoch, 2007: Variability in the subtropical tropical cells and its effect on near-surface temperature of the equatorial Pacific: A model study. *Ocean Sci.*, **4**, 73–88.
- McCreary, J., and P. Lu, 1994: Interactions between the subtropical and equatorial ocean circulations: The subtropical cell. *J. Phys. Oceanogr.*, **24**, 466–497.
- , —, and Z. Yu, 2002: Dynamics of the Pacific subsurface countercurrents. *J. Phys. Oceanogr.*, **32**, 2379–2404.
- McDougall, T. J., 1989: Streamfunctions for the lateral velocity vector in a compressible ocean. *J. Mar. Res.*, **47**, 267–284.
- McPhaden, M. J., and D. Zhang, 2002: Slowdown of the meridional overturning circulation in the upper Pacific Ocean. *Nature*, **415**, 603–608.
- , and —, 2004: Pacific Ocean circulation rebounds. *Geophys. Res. Lett.*, **31**, L18301, doi:10.1029/2004GL020727.
- Melet, A., L. Gourdeau, and J. Verron, 2010: Variability in Solomon Sea circulation derived from altimeter data. *Ocean Dyn.*, **60**, 883–900.
- Montes, I., F. Colas, X. Capet, and W. Schneider, 2010: On the pathways of the equatorial subsurface currents in the eastern equatorial Pacific and their contributions to the Peru–Chile Undercurrent. *J. Geophys. Res.*, **115**, C09003, doi:10.1029/2009JC005710.
- Montgomery, R. B., 1937: A suggested method for representing gradient flow in isentropic surfaces. *Bull. Amer. Meteor. Soc.*, **18**, 210–212.
- Moore, G. W. K., and I. A. Renfrew, 2002: An assessment of the surface turbulent heat fluxes from the NCEP–NCAR reanalysis over the western boundary currents. *J. Climate*, **15**, 2020–2037.
- Munk, W. H., and C. Wunsch, 1998: Abyssal recipes II: Energetics of tidal and wind mixing. *Deep-Sea Res.*, **45**, 1977–2010.
- Newman, M., P. D. Sardeshmukh, and J. W. Bergman, 2000: An assessment of the NCEP, NASA, and ECMWF reanalyses over the tropical west Pacific warm pool. *Bull. Amer. Meteor. Soc.*, **81**, 41–48.
- Pegion, P. J., M. A. Bourassa, D. M. Legler, and J. J. O’Brien, 2000: Objectively derived daily “winds” from satellite scatterometer data. *Mon. Wea. Rev.*, **128**, 3150–3168.
- Potemra, J. T., and N. Schneider, 2007: Interannual variations of the Indonesian Throughflow. *J. Geophys. Res.*, **112**, C05035, doi:10.1029/2006JC003808.
- Renfrew, I. A., G. W. Moore, P. S. Guest, and K. Bumke, 2002: A comparison of surface layer and surface turbulent flux observations over the Labrador Sea with ECMWF analyses and NCEP reanalyses. *J. Phys. Oceanogr.*, **32**, 383–400.
- Risien, C. M., and D. B. Chelton, 2008: A global climatology of surface wind and wind stress fields from eight years of QuikSCAT scatterometer data. *J. Phys. Oceanogr.*, **38**, 2379–2413.
- Roemmich, D. H., and J. Gilson, 2009: The 2004–2008 mean and annual cycle of temperature, salinity, and steric height in the global ocean from Argo Program. *Prog. Oceanogr.*, **82**, 81–100.
- , and —, 2011: The global ocean imprint of ENSO. *Geophys. Res. Lett.*, **38**, L13606, doi:10.1029/2011GL047992.
- Rouault, M., C. J. C. Reason, J. R. E. Lutjeharms, and A. C. M. Beljaars, 2003: Underestimation of latent and sensible heat fluxes above the Agulhas Current in NCEP and ECMWF analyses. *J. Climate*, **16**, 776–782.
- Santoso, A., W. Cai, M. H. England, and S. J. Phipps, 2011: The role of the Indonesian Throughflow on ENSO dynamics in a coupled climate model. *J. Climate*, **24**, 585–601.
- Sato, K., and T. Suga, 2009: Structure and modification of the South Pacific Eastern Subtropical Mode Water. *J. Phys. Oceanogr.*, **39**, 1700–1714.
- Shinoda, T., H. Hendon, and J. Glick, 1999: Intraseasonal surface fluxes in the tropical western Pacific and Indian Oceans from NCEP reanalyses. *Mon. Wea. Rev.*, **127**, 678–693.

- Silva, N., and S. Neshyba, 1979: On the southernmost extension of the Peru–Chile Undercurrent. *Deep-Sea Res.*, **26**, 1387–1393.
- Sokolov, S., and S. Rintoul, 2000: Circulation and water masses of the southwest Pacific WOCE section P11, Papua New Guinea to Tasmania. *J. Mar. Res.*, **58**, 223–268.
- Song, Q., G. A. Vecchi, and A. J. Rosati, 2007: The role of the Indonesian Throughflow in the Indo-Pacific climate variability in the GFDL coupled climate model. *J. Climate*, **20**, 2434–2451.
- Sprintall, J., S. E. Wijffels, R. Molcard, and I. Jaya, 2009: Direct estimates of the Indonesian Throughflow entering the Indian Ocean: 2004–2006. *Deep-Sea Res.*, **114**, C07001, doi:10.1029/2008JC005257.
- Tillinger, D., and A. L. Gordon, 2009: Fifty years of the Indonesian Throughflow. *J. Climate*, **22**, 6342–6355.
- Tsuchiya, M., 1981: The origin of the Pacific equatorial 13°C water. *J. Phys. Oceanogr.*, **11**, 794–812.